

RESEARCH OUTPUTS / RÉSULTATS DE RECHERCHE

Efficiency enhancement of perovskite solar cells based on opal-like photonic crystals

Lobet, Michaël; Piron, Pierre; Dewalque, Jennifer; Maho, Anthony; Deparis, Olivier; Henrist, Catherine; Loicq, Jérôme

Published in:
Optics Express

DOI:
[10.1364/oe.27.032308](https://doi.org/10.1364/oe.27.032308)

Publication date:
2019

Document Version
Publisher's PDF, also known as Version of record

[Link to publication](#)

Citation for published version (HARVARD):

Lobet, M, Piron, P, Dewalque, J, Maho, A, Deparis, O, Henrist, C & Loicq, J 2019, 'Efficiency enhancement of perovskite solar cells based on opal-like photonic crystals', *Optics Express*, vol. 27, no. 22, pp. 32308-32322. <https://doi.org/10.1364/oe.27.032308>

General rights

Copyright and moral rights for the publications made accessible in the public portal are retained by the authors and/or other copyright owners and it is a condition of accessing publications that users recognise and abide by the legal requirements associated with these rights.

- Users may download and print one copy of any publication from the public portal for the purpose of private study or research.
- You may not further distribute the material or use it for any profit-making activity or commercial gain
- You may freely distribute the URL identifying the publication in the public portal ?

Take down policy

If you believe that this document breaches copyright please contact us providing details, and we will remove access to the work immediately and investigate your claim.



Efficiency enhancement of perovskite solar cells based on opal-like photonic crystals

MICHAËL LOBET,¹ PIERRE PIRON,¹ JENNIFER DEWALQUE,²
ANTHONY MAHO,² OLIVIER DEPARIS,³ CATHERINE HENRIST,² AND
JÉRÔME LOICQ^{1,*}

¹Centre Spatial de Liège, Avenue du Pré-Aily, B-4031 Angleur, Belgium

²University of Liège, CESAM-GREENMAT, Allée du Six-Aout 13, B-4000 (Sart Tilman), Belgium

³Solid-State Physics Laboratory, University of Namur, Rue de Bruxelles 61, B-5000 Namur, Belgium
j.loicq@uliege.be

Abstract: Perovskite solar cells have shown a tremendous interest for photovoltaics since the past decade. However, little is known on the influence of light management using photonic crystals inside such structures. We present here numerical simulations showing the effect of photonic crystal structuring on the integrated quantum efficiency of perovskite solar cells. The photo-active layer is made of an opal-like perovskite structure (monolayer, bilayer or trilayer of perovskite spheres) built in a TiO_2 matrix. Fano resonances are exploited in order to enhance the absorption, especially near the bandgap of perovskite material. The excitation of quasi-guided modes inside the absorbing spheres enhances the integrated quantum efficiency and the photonic enhancement factor. More specifically, a photonic enhancement factor as high as 6.4% is predicted in the case of spheres monolayer compared to an unstructured perovskite layer. The influences of sphere's radius and incident angle on the absorbing properties are also estimated. Those numerical results can be applied to the nascent field of photonic structuring inside perovskite solar cells.

© 2019 Optical Society of America under the terms of the [OSA Open Access Publishing Agreement](#)

1. Introduction

For decades, the photovoltaic (PV) market is dominated by crystalline Si solar cells with power conversion efficiency (PCE) above 25 % [1]. An attractive way to reduce the costs and material usage is to develop thin-film technologies [2,3]. It can potentially boost the market launch of such PV devices. Another advantage of thin-film technologies is the smaller diffusion length for the charge carriers allowing to use absorbing materials of lower crystallinity. However, since the photon penetration depth is bigger than the film thickness, especially near the bandgap, the PCE is drastically reduced. This problem calls for efficient light management in order to enhance photon absorption within the thin photo-active layer. Various photonic concepts have been developed to solve this issue, including anti-reflective coating, back-reflectors or random surface texturing [2–5]. Those concepts are intrinsically non-resonant and lead therefore to a spectrally broadband enhancement. Due to their intrinsic capabilities to manage the flow of light [6], photonic crystals (PC) have been recently studied for enhancing photon harvesting in thin-film solar cells. The photonic bandgap of PC is useful to replace back-reflectors in PV devices [7,8]. Another strategy using PC is to excite quasi-guided resonances inside the photo-active layer [9–14]. It allows a greater electromagnetic field concentration inside the desired layer and, in such a way, enhances the photo-current. This resonant phenomenon is also described as Fano resonance which consists in interference between broadband and resonant scattering processes [15,16]. Fano resonances are well studied in the literature and, for example, both arrays of dielectric spheres, sometimes called 3D metacrystals [16], and opals demonstrated they can support Fano resonances [16–21]. Interestingly, one can connect Fano resonances to Mie scattering by spherical particles [22]. Indeed, resonant Mie scattering from dielectric spheres can be seen as an infinite series of Fano resonances [23,24].

All current PV technologies (Si, organic, dye-sensitized, CIGS, etc) are impacted by the beneficial effects of photonic crystals on PCE [10,14,25–28]. In spite of that, only little is known so far on the photonic gain obtained from PC structuring on fast growing technology of organic-inorganic perovskite solar cells (PSC). The PCE in that technology has increased from 2.2% [29] to 24.2% [1] in only one decade, draining a lot of interest in the PV community. The key advantages of perovskites are their large optical absorption coefficient, suitable bandgap for PV, long carrier lifetime and diffusion length, and low fabrication costs [30–32]. Most of the best PSC use methylammonium lead triiodide ($CH_3NH_3PbI_3$) which has a bandgap around 800 nm (1.55 eV). Absorption falls very sharply around this wavelength [30,33]. In order to overcome this issue and to improve the overall PCE in PSC, we focus here on the nascent field of light management using photonic crystals in perovskite solar cells [34–41]. References [34,35,38] reported successful preparation of inverse opal perovskite films that may lead to improve PCE while ref [36] demonstrated the fabrication of an ordered macroporous perovskite monolayer using a polystyrene microsphere template. As demonstrated in [36] by Chen et al., a pore radius larger than 100 nm guaranteed sufficient light harvesting while the optimum radius was 200 nm. The PCE of this optimized structure is equal to 11.7% which is enhanced with respect to an island-like perovskite film having a PCE of 5.6%. A PCE of 17.1% was also achieved with a 600 nm mesoscopic inverse opal film with a three-dimensionally interconnected porous structure (ref [37]). Interestingly, Schmager and co-workers [40,41] experimentally demonstrated that a 2D periodic array of holes inside perovskite can foster absorption via the coupling to quasi-guided modes in thin-film perovskite solar cells. Their strategy yielded an improvement by 5.6% in short-circuit current and by 2% in PCE, as compared to planar structures. Herein, we first discuss figures of merit and the numerical method used in our calculations. We then numerically analyze PSC made of either homogeneous unstructured layers or opal-like photonic crystal slabs consisting of monolayers, bilayers and trilayers of perovskite spheres inside a TiO_2 host matrix. We evidence quasi-guided resonances as the physical mechanism responsible for the absorption enhancement and determine the optimal structure parameters. A particular attention is paid to parasitic absorption throughout this study. Finally, the angular dependence of the integrated quantum efficiency of the optimal structures is examined.

2. Photonic structures and materials

The different photonic structures under investigation are described in Fig. 1. They correspond to the final assembly of a realistic PSC. The role of the photonic structuring of the photo-active layer will be examined hereafter. In our simulations, the incident medium is a semi-infinite non-dispersive uniform glass material with a refractive index n_{inc} of 1.5. A uniform 400 nm-thick Fluorine-doped Tin Oxide (FTO) transparent conducting electrode layer and a uniform 40 nm-thick TiO_2 layer (hole blocking layer) are placed above the photo-active perovskite layer [42]. The complex refractive indices of FTO and TiO_2 are taken from [43]. It should be noted that TiO_2 has a bandgap around 385 nm and consequently does not absorb in the visible range. Nevertheless, as shown later, below 385 nm, TiO_2 produces some parasitic absorption, i.e. light being lost for absorption in the photo-active material.

The photo-active layer is either an unstructured, homogeneous layer of methylammonium lead triiodide ($MAPbI_3$) perovskite (Fig. 1(a)) or a structured perovskite layer of the same chemical composition (Fig. 1(b)). The structuring consists of N layers ($N = 1, 2, 3$) of perovskite spheres of radius R embedded in a TiO_2 host matrix (electron-collecting electrode). The spheres are arranged according to a face centered cubic close-packed structure with an ABC stacking (filling fraction of 0.74). The finite N -layers arrangement corresponds to the N first crystallographic planes of an opal photonic crystal (N tending towards infinity) [6].

The spread of reported values for the refractive index of the $MAPbI_3$ perovskite is quite large in the literature [30–33,42]. This might be due to non-uniform thickness of deposited layers,

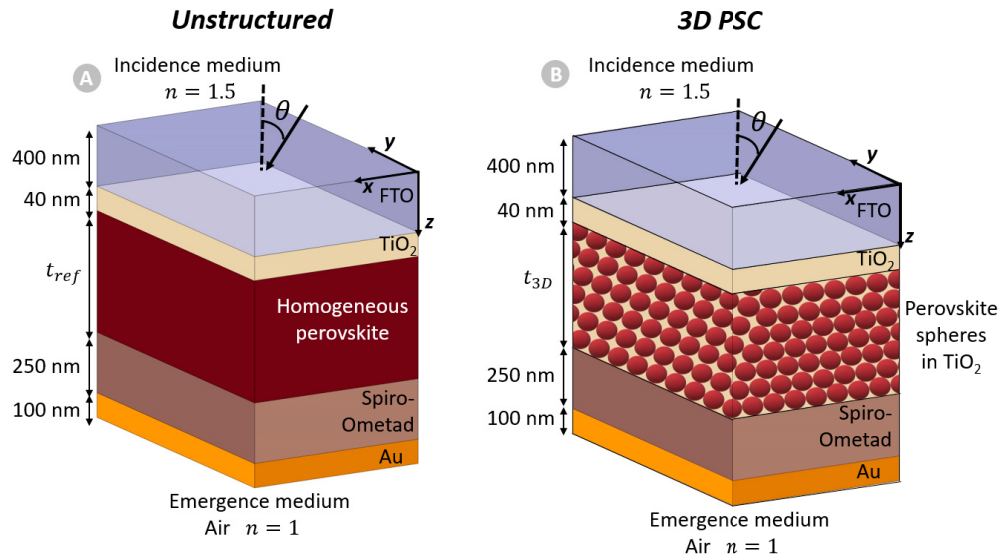


Fig. 1. Schematic of unstructured (a) and opal-like photonic crystal (b) perovskite solar cells. Incidence medium refractive index is equal to 1.5 (glass). FTO layer is 400 nm-thick and TiO_2 layer is 40 nm-thick. Thicknesses of the unstructured perovskite (t_{ref}) and structured layers (t_{3D}) are varied, while the thicknesses of Spiro-OMeTAD (250 nm) and gold (100 nm) layers are fixed.

to the presence of PbI_2 or to some material anisotropy appearing during the material synthesis. We decided to take data from Löper et al. [33] described as the "middle of the road" and as "reasonable data" among the diversity of reported refractive indices [30]. The photon penetration depth δ_p is defined as $1/\delta_p = 4\pi Im(n)/\lambda$ (n being the refractive index of the considered layer and λ the vacuum wavelength) and is represented on Fig. 2 for $MAPbI_3$ perovskite from Löper's data. The imaginary part of the refractive index $Im(n)$ is non-zero between 310 nm and 800 nm. One can clearly notice the bandgap at 800 nm and the subsequent increase of the penetration depth at longer wavelengths.

A hole transporting layer made of Spiro-OMeTAD ($C_{81}H_{68}N_4O_8$), with a thickness of 250 nm is inserted between the photo-active layer and the gold counter-electrode. The latter is 100 nm-thick and also acts as back-reflector (Fig. 1). The complex refractive indices from Spiro-OMeTAD and gold are taken from [43] and [44] respectively. One should note that the thicknesses of blocking TiO_2 , Spiro-OMeTAD and gold layers correspond to optimal thicknesses evidenced in literature [42,45]. The different layers described above constitute the unit cell (UC) of the PSC. The basis vectors form a (virtual) square array in the unstructured case (Fig. 1(a)) and an hexagonal closed-packed array in the structured case (Fig. 1(b)).

The structured perovskite layer is synthesized as follows. First, inverse opal TiO_2 porous films are prepared from wet routes through templating strategies with polystyrene (PS) beads as structuring agent. In a typical procedure, PS beads are spin-coated on top of a transparent conductive substrate and form an hexagonal compact arrangement. Second, a TiO_2 precursor solution is further infiltrated within the PS beads layer. The sample is then calcined in order to crystallize TiO_2 and to remove the beads. Beads elimination leads to spherical pores network formation within the TiO_2 layer. Finally, these spherical pores are filled with perovskite in order to achieve the structured perovskite layer. This fully justifies the realistic approach of the photonic structuring presented in this numerical study.

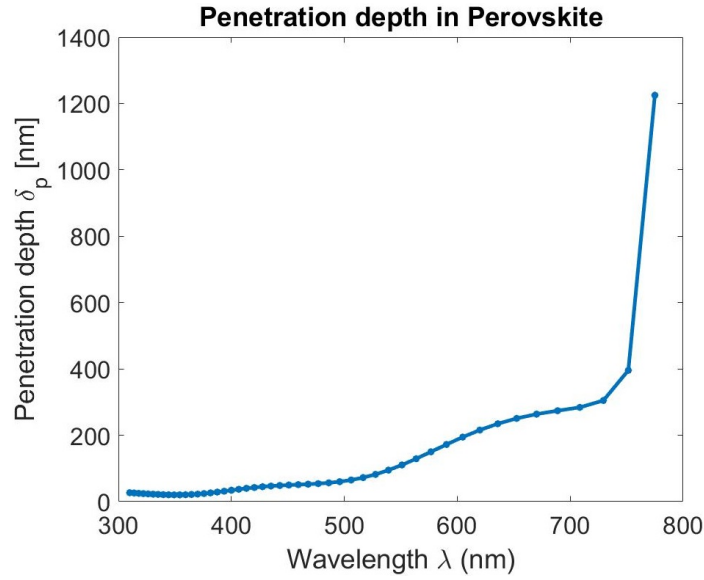


Fig. 2. Penetration depth δ_p of methylammonium lead triiodide (MAPbI_3) perovskite coming from Löper's data [33]. The imaginary part of the refractive index is non-zero between 310 nm and 800 nm.

3. Numerical methods and figures of merit

Numerical simulations were performed in order to calculate the enhancement of absorption inside the structured PSC. The stratified and periodic aspects of the geometry, in particular the inclusion of photonic structuring inside the photo-active layer, are perfectly suitable for the Rigorous Coupled Wave Analysis (RCWA) method [46,47]. This method assumes a lateral periodicity of the electric permittivity and solves Maxwell equations exactly. The permittivity and the electromagnetic fields are developed in truncated 2D Fourier series. The number of plane waves used in the truncated series is the key parameter for numerical convergence. Since the refractive index mismatch between the different materials composing the photonic structures is quite low and the spheres are touching each other, 7×7 plane waves along the x and y directions are sufficient in order to obtain converged results here. The flux of the Poynting vector is calculated in both the incidence and emergence media in order to get total reflectance $R(\lambda)$, i.e. including all diffraction orders, and total transmittance $T(\lambda)$, at each wavelength λ . The global absorptance $A_g(\lambda)$ is then deduced from the energy conservation law:

$$A_g(\lambda) = 1 - R(\lambda) - T(\lambda). \quad (1)$$

It should be noted that the combination of a highly absorptive perovskite layer and a 100 nm-thick gold layer completely inhibits the transmittance ($T(\lambda) = 0$).

Two figures of merit are defined in order to characterize the absorption properties of the PSC and to evidence the effect of photonic structuring. First, we use the integrated quantum efficiency (iQE) [48] η representing the percentage of incident photons that are absorbed in the whole structure [49,50]. This quantity is given by the ratio of the spectrally integrated absorbed photon flux ϕ_A to the spectrally integrated incident photon flux ϕ_{inc} :

$$\eta = \frac{\phi_A}{\phi_{inc}} = \frac{\int_{\lambda_{min}}^{\lambda_{max}} \frac{\lambda}{hc} S(\lambda) A_g(\lambda) d\lambda}{\int_{\lambda_{min}}^{\lambda_{max}} \frac{\lambda}{hc} S(\lambda) d\lambda} \quad (2)$$

where h is the Planck constant, c the speed of light in vacuum, $S(\lambda)$ the normalized solar spectrum AM1.5G, $\lambda_{min} = 310$ nm and $\lambda_{max} = 800$ nm corresponding respectively to the lower bound of the solar spectrum and to the perovskite band gap (Fig. 2 and [33]). It is noteworthy that we focus here on the optical properties only, and that no electrical properties of the PSC are considered in the present study. However, in a solar cell, carrier transport and recombination process will ultimately set the performance in term of PCE.

For the sake of evidencing the beneficial effect of photonic structuring of the photo-active layer, a second figure of merit, which gives a fair comparison between the structured (3D PC) and unstructured PSC, is considered. We suppose that each absorbed photon generates an electron-hole pair in both cases. This hypothesis allows us to evaluate the enhancement of the generation of photo-electrons due to the photonic structuring in comparison with an equivalent unstructured photonic slab. The photonic enhancement factor G_{phot} is defined as

$$G_{phot} = \frac{\phi_{3D} - \phi_{hom}}{\phi_{hom}} \times 100 \quad (3)$$

where ϕ_{3D} and ϕ_{hom} are, respectively, the spectrally integrated absorbed photon flux in the 3D photonic structure and in the equivalent unstructured layer. The thickness of the planar unstructured perovskite layer is chosen in such a way that the volume quantity of perovskite material is identical in both structured and unstructured PSC. In the later, the equivalent thickness is $t_{eq} = \frac{V_{pero}}{V_{UC}} \times t_{3D}$ where V_{pero} is the volume of the perovskite spheres, V_{UC} the volume of the unit cell and t_{3D} the thickness of the structured PC layer (Fig. 1).

The global absorptance calculated in eq.1 corresponds to the absorption occurring in the whole solar cell, i.e. it includes both the useful absorption responsible for the generation of photo-electrons inside perovskite material and the parasitic absorption inside the other layers. Therefore, a great care must be taken on the exact location of the absorption process. In order to map the absorption and the electron-hole pair generation as well as to quantify the absorption within the photo-active layer, we calculate the local absorptance at a particular position \mathbf{r} from the local value of the electric field $\mathbf{E}(\mathbf{r}, \omega)$ resulting from the RCWA calculations. Starting from Poynting's theorem and the method developed in [51], the absorbed power P_a in a volume V is given by

$$P_a = \frac{\varepsilon_0 \omega}{2} \int_V \text{Im}(\varepsilon(\mathbf{r}, \omega)) |\mathbf{E}(\mathbf{r}, \omega)|^2 dV \quad (4)$$

with $\varepsilon(\mathbf{r}, \omega)$ the local complex electric permittivity. By normalizing the absorbed power P_a to the incident power P_i , one obtains the local absorptance $A_{loc}(\mathbf{r}, \omega) = P_a/P_i$. The local absorptance A_{loc} , once it is integrated on the whole structure, must converge towards the global absorptance A_g obtained via the conservation of energy. We should note that the developed formula of local absorptance shows direct proportionality to δz , the discretization steps in the z direction and inverse proportionality to N_x and N_y , the number of points taken in the x and y directions [51]. Since the electric field is homogeneous along x and y for each z value in an unstructured PSC, the values of N_x and N_y are not critical in this case and the local absorptance A_{loc} converges rapidly towards the global absorptance A_g . However, in a 3D PC, the discretization of the structure and the number of plane waves used in the Fourier expansion of the electric permittivity may introduce some numerical inaccuracies in the calculation of the local absorptance. Moreover, if sharp resonances resulting from a complex photonic structure, are present in the spectrum, the numerical error on the local absorptance can be significant. For the sake of keeping reasonable computing time and using efficiently memory resources, the local absorptance calculations for 3D PC will be considered as an approximate numerical tool to help understanding where parasitic absorption occurs. We can nevertheless quantify the numerical convergence of local absorptance calculations. To this aim, we introduce the deviation parameter $\Delta = \left| \int A_{loc} dV - A_g \right|$ to provide

an idea of the reliability of our calculations. In order to ensure reliable results in the present study, the maximum deviation parameter Δ that we authorize on local absorptance never exceeds 2.0%. This percentage is a fair trade-off between accuracy and reasonable use of calculation resources. All calculations are performed at normal incidence except in the last subsection where the angular behaviour is investigated.

4. Benefit of the photonic structuring

4.1. Unstructured perovskite solar cells

Unstructured perovskite solar cells, corresponding to planar perovskite layers in the (x, y) plane (Fig. 1(a)), will serve as a reference throughout the study. First, let us consider the whole cell without perovskite ($t_{ref} = 0$). The absorptance spectrum (Fig. 3(a), yellow curve) exhibits a non-negligible parasitic absorption with an equivalent integrated quantum efficiency η of 41.8%. As we will show it further, it is mainly due to the absorption in the FTO, TiO_2 and gold layers. Increasing the perovskite thickness leads to an increased iQE followed by a saturation (Fig. 3(b)). A 150 nm-thick perovskite layer provides $\eta = 80.6\%$ while a 600 nm-thick layer allows to achieve $\eta = 93.3\%$. Thicker unstructured perovskite layers only increase the iQE marginally, the remaining energy being lost by multiple reflections. The small noticeable oscillations in the iQE curve are due to Fabry-Perot interferences within the unstructured slab.

As seen on Fig. 3(a), the absorptance spectrum of a 600 nm-thick unstructured layer provides a relatively high and broadband absorption with a rapid fall of the absorptance above $\lambda \cong 750$ nm. This diminution is related to the increased penetration depth δ_p (Fig. 2). At 750 nm, δ_p is estimated to be 395 nm. The importance of the gold back-reflector is also highlighted in Figs. 3(a) and 3(c). A single pass in perovskite layer (600 nm thick), i.e. without gold back-reflector, has an iQE $\eta = 87.4\%$ while a double pass in perovskite layer, i.e. with gold back-reflector, has an iQE $\eta = 93.3\%$. One can distinguish that the enhancement is mainly present at long wavelengths. It can be understood by looking at the local absorptance A_{loc} integrated within the (x, y) plane, as a function of the thickness z (Fig. 3(c) with $\lambda = 600$ nm). If the gold back-reflector is not present, light is mainly absorbed within the perovskite layer. The absorptance follows an exponential decay as predicted by Beer-Lambert law. Slight oscillations in the perovskite region are due to the back-reflection on the Spiro-OMeTAD layer. However, with the gold back-reflector, larger oscillations appear in the perovskite layer. Those are due to stronger interference inside the perovskite layer, which favors the absorption near the interface with the Spiro-OMeTAD layer. The absorption maxima are separated by $\lambda/2n$ ($\lambda/2n'$, n (n') being the refractive index of the perovskite (FTO) layer). Furthermore, this interference process is observed on the local absorptance map (Fig. 3(d)). The integration of the local absorptance within different layers in the unstructured PSC provides interesting and reliable results ($\Delta = 0.1\%$) on the role of the different layers. At $\lambda = 600$ nm, in the double pass structure, the FTO layer absorbs 5.8%, the TiO_2 layer does not absorb light at all, the active perovskite layer absorbs 89.2% and the Spiro-OMeTAD and gold layers absorb 0.5% each. This quantifies the parasitic absorptance to roughly 6.8% at 600 nm. The remaining energy is simply lost by Fresnel reflections. A similar analysis can be done at 360 nm, i.e. below the TiO_2 bandgap. It reveals that the FTO layer absorbs 12.7%, the 40 nm-thick TiO_2 absorbs 1.9% while the perovskite layer absorbs the remaining part up to 82.3% ($\Delta = 0.5\%$). The Spiro-OMeTAD and gold layer do not absorb due to the small penetration depth of perovskite ($\delta_p = 17$ nm) at 360 nm. One can note that about 15% of the incident light is lost in the first two layers. Furthermore, about 20% of the incoming energy above the perovskite bandgap (800 nm) is converted into parasitic absorption. At 837 nm for example, the FTO absorbs 18.9% while the gold layer absorbs 2.6% ($\Delta = 0.1\%$) for a global absorptance equal to 21.5%. One should note that a 600 nm-thick layer corresponds to a thickness that maximizes the useful absorption in an unstructured PSC, with a high iQE.

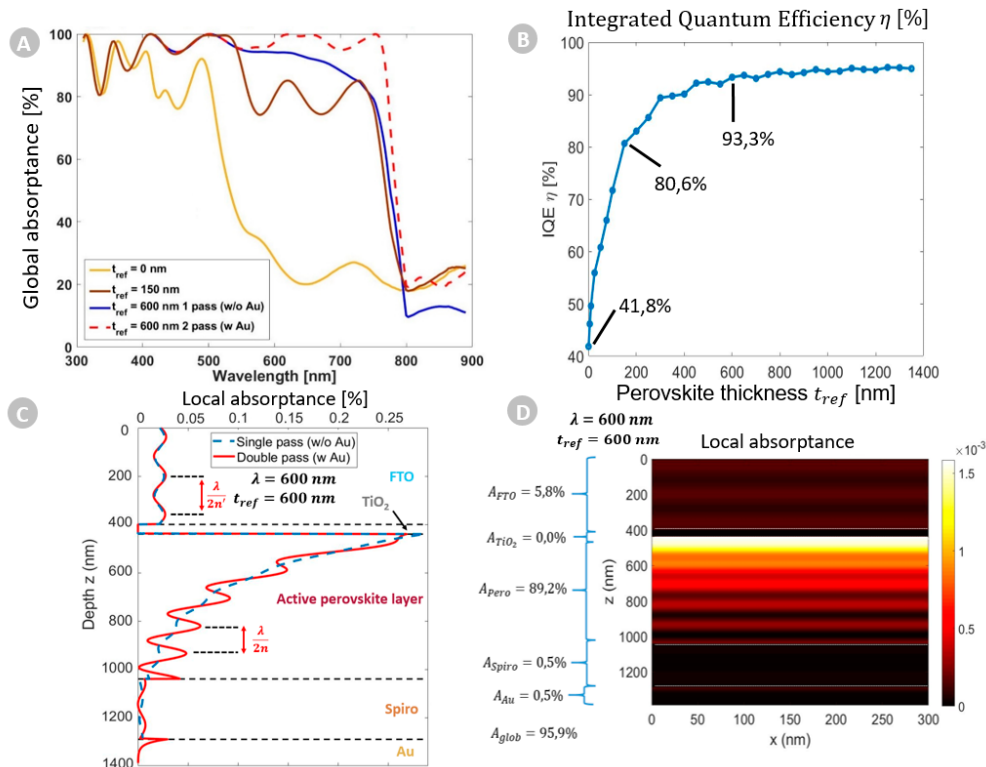


Fig. 3. Unstructured perovskite solar cells. (a) Absorbance spectra with no perovskite (yellow line), 150 nm-thick perovskite layer (brown line), 600 nm-thick perovskite layer in single pass (no back-reflector) (blue line) and 600 nm-thick perovskite layer in double pass (with gold back-reflector) (red dotted line), (b) Integrated quantum efficiency η as a function of perovskite layer thickness t_{ref} . (c) Local absorbance (integrated in the (x, y) plane) as a function of depth z at $\lambda = 600$ nm, (d) Local absorption map at $\lambda = 600$ nm for a 600 nm-thick layer inserted in the complete PSC.

4.2. Monolayer of perovskite spheres in an hexagonal array

In order to investigate the effect of photonic structuring of the perovskite layer, we designed a photo-active layer with a single-layer hexagonal array of perovskite spheres having a radius R inside a TiO_2 matrix. Taking, for example, different radii of 175 nm, 200 nm and 475 nm, we can clearly distinguish resonant modes in the absorbance spectrum (Fig. 4) which enhance the absorption especially near the perovskite bandgap. These resonant modes are obviously absent in the absorbance spectrum of the unstructured counterparts (dashed curves in Fig. 4, calculated with t_{eq} defined above). These modes correspond to quasi-guided resonances inside the structure with light propagating along the (x, y) plane. They are able to couple with external radiation and to strongly confine the electromagnetic power within the photonic structure [16,19,52–54]. They are characterized by a spectrum with sharp resonant features (Fano resonances) superimposed upon a smoothly varying background that resembles Fabry-Perot oscillations. Propagation through such a 3D photonic structure results from an interference process between a direct pathway where the incident light interacts with a uniform dielectric background and an indirect pathway where the remaining portion of the incident light excites the quasi-guided resonances [52].

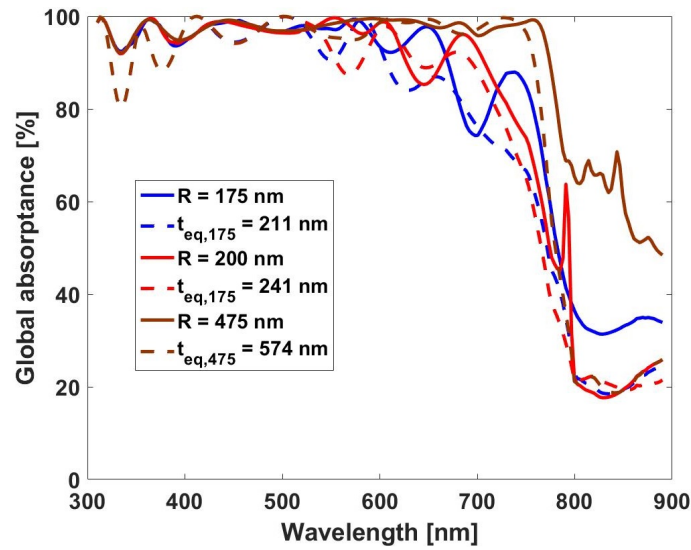


Fig. 4. Global absorbance spectra of a PSC with a single layer array of spheres having a radius $R = 175$ nm (blue lines), $R = 200$ nm (red lines) or $R = 475$ nm (brown lines) and the equivalent PSC with unstructured perovskite layer (red dashed lines).

In order to confirm this confinement mechanism and to reveal the appearance of quasi-guided modes, we will consider first a simplified model consisting of non-dispersive, non-absorbing spheres arranged in a hexagonal 2D array inside a non-dispersive slab. Then we examine the field patterns and the local absorbance of a resonant mode. Let us first establish a simplified model made of free-standing non-dispersive perovskite spheres ($R = 175$ nm) within a non-dispersive slab of TiO_2 (Fig. 5(a)). The refractive indices are chosen as $n_{spheres} = 2.4055$ and $n_{bgd} = 2.1907$ which correspond to the mean refractive indices of perovskite and TiO_2 , respectively, over the spectral region of interest. The imaginary part of the refractive indices are intentionally set equal to zero. The latter condition is justified by our aim to study pure light trapping mechanisms (enhanced $|E|^2$ in eq.4). Consequently no absorption occurs in the following calculations.

As shown by López-García et al.[54], a 2D array of dielectric spheres is able to confine light inside a photonic slab. The transmittance and reflectance spectra (Fig. 5(b)) corresponding to our simplified model (Fig. 5(a)) clearly exhibit sharp peaks, i.e. Fano resonances. The slowly varying background (dashed lines) is perfectly reproduced when we use an effective (volume averaged) refractive index, $n_{eff} = \frac{\pi}{3\sqrt{3}}n_{spheres} + (1 - \frac{\pi}{3\sqrt{3}})n_{bgd}$ and a layer thickness of $2R$ [54]. Moreover, the introduction of adjacent layers in order to reconstruct the initial PSC inevitably reduces the confinement capability of the photonic structure because of the radiative losses within these adjacent layers. Indeed, mismatch of refractive indices between the 3D PC (perovskite/ TiO_2) layer and cladding layers is substantially lowered compared to the same layer placed in air. Consequently, the energy leaks within the surrounding layers results in a spectral shift and a broadening of the resonant peaks [54].

Let us introduce the dispersive and absorbing properties of the perovskite material. We analyze the profile of the integrated local absorbance as a function of depth z (Fig. 6(a)) and the map of the local absorbance (Fig. 6(b)) at a specific resonant wavelength in order to confirm our quasi-guided resonance interpretation. At the wavelength $\lambda = 738$ nm ($R = 175$ nm, see Fig. 4), the local absorption profile (Fig. 6(a)) is totally different from a Beer-Lambert profile, as evidenced previously in the unstructured photonic slab. This result confirms that an important part of the electromagnetic radiation is confined inside the photo-active perovskite

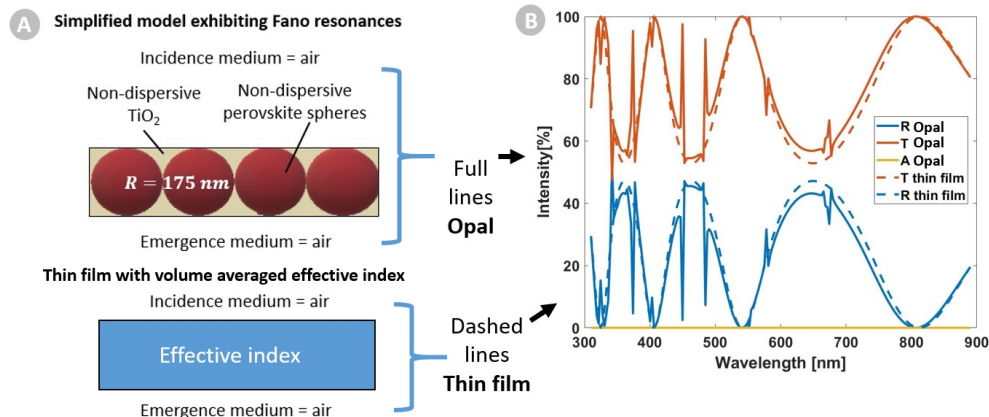


Fig. 5. (a) Schematic of the simplified model consisting of free-standing non-dispersive, non-absorbing perovskite spheres ($R = 175 \text{ nm}$) arranged in a hexagonal 2D array within a non-dispersive slab of TiO_2 , (b) Reflectance (R), transmittance (T) and absorbance (A) of perovskite spheres inside TiO_2 slab surrounded by air. The dashed lines corresponds to reflectance and transmittance of a homogeneous slab made of a volume averaged effective index, reproducing the slowly varying background. Fano resonances are seen as sharp features in the spectra.

layer. However, an interference pattern is also observed, which comes from reminiscence of the direct pathway where light interacts with the dielectric slab as a whole. The Fano resonance excites a quasi-guided mode within the photo-active material as seen on Fig. 6(b) at a depth of $z \cong 600 \text{ nm}$. This confinement mechanism enables an enhancement of absorption within the PSC. Although Fano resonances were already evidenced in 3D dielectric metacrystals [17,18] or in dielectric opals [19–21], it is the first time, to the best of our knowledge, that the Fano resonances are exploited to enhance the absorption near the bandgap of perovskite materials.

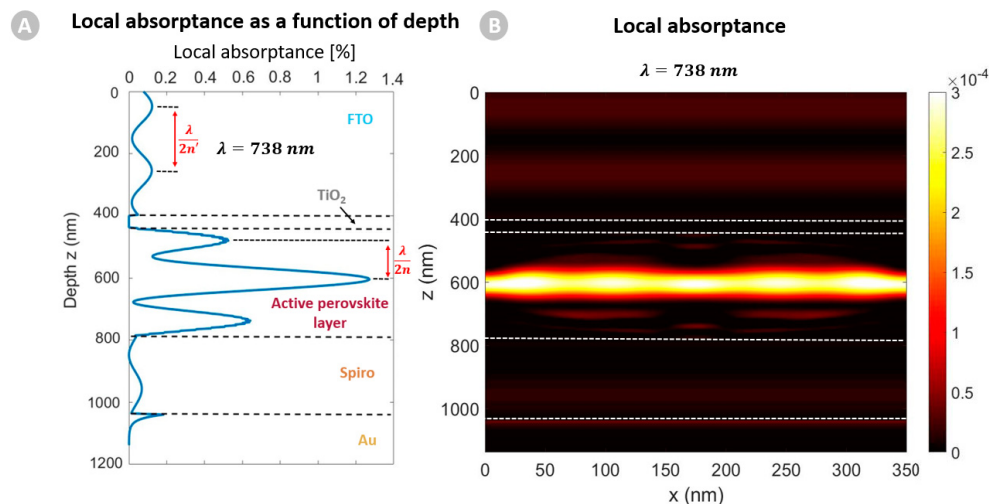


Fig. 6. (a) Local absorbance as a function of depth for a resonant wavelength $\lambda = 738 \text{ nm}$ of an array of spheres with radius $R = 175 \text{ nm}$. (b) Local absorbance map for a resonant wavelength $\lambda = 738 \text{ nm}$ of an array of spheres with radius $R = 175 \text{ nm}$. Those figures reveal the presence of a quasi-guided mode.

Furthermore, one can also estimate the parasitic absorption in the 3D photonic crystal PSC by spatially integrating the absorptance map (Fig. 6(b)) over the layer of interest. For example, at resonant Fano wavelength of $\lambda = 738$ nm, the absorptance is estimated to be 78.6% ($\Delta = 2.0\%$) distributed as 66.0% within the perovskite spheres and 12.6% of parasitic absorptance (8.8% absorbed inside the FTO layer). At a wavelength closer to the bandgap (790 nm) the absorptance is 29.1% ($\Delta = 0.1\%$) with 11.9% in the perovskite spheres and 17.2% of parasitic absorption (13.3% within the FTO layer). Above the perovskite bandgap (800 nm), the absorption is mainly due to the FTO layer since, at 829 nm, $A_{FTO} = 17.1\%$ and $A_{Au} = 2.6\%$ ($\Delta = 0.1\%$).

4.3. Effect of the number of layers and the radius of the spheres

As we showed above, introducing a monolayer of perovskite spheres increases the absorption by exciting quasi-guided resonances [16,19,52–54]. Since the physical mechanism of light confinement is now well understood, we analyze hereafter the effect of increasing the number of layers ($N = 1, 2, 3$) and of increasing the radius of the spheres R on the two figures of merit, i.e. iQE η and photonic enhancement factor G_{phot} . The radius R varies from 25 nm up to 1100 nm by steps of 25 nm. Increasing the sphere radius has a double impact on the absorption properties. First, it increases the number of Fano resonances inside the PC. Second, it provides more absorbing material and therefore the probability for light to be absorbed is enhanced. The photonic enhancement factor G_{phot} is positive only if $R > 100$ nm. Below this radius threshold, there is not enough absorbing material and Fabry-Perot oscillations occur more hardly at visible wavelengths. The interference mechanism responsible for Fano resonance between direct and indirect pathways is therefore reduced. This is fully consistent with the findings of ref [36] where pores larger than 100 nm were reported to guarantee sufficient light harvesting. We note that, as R is varied, both iQE and G_{phot} present an oscillatory behaviour due to these interferences (Fig. 7). The photonic enhancement factor peaks at specific radii and shows a damping at large radii. Larger radii induce higher iQE but correspond to a relatively smaller photonic enhancement factor. The spheres arrangement, at the relevant wavelength scale, being more and more alike to a uniform homogeneous layer when the sphere radius is large, this geometrical effect reduces the impact of the photonic structuring. It also explains why a 3D PC composed of three layers has a faster damping of G_{phot} while having the best iQE among the tested configurations. For this reason, using a higher number of layers will not improve the photonic enhancement factor. According to the figure of merit we search to enhance, we will choose one of the different configurations. We choose to focus on the photonic enhancement factor since it assesses the enhancement of absorption due to photonic structuring. The champion configurations for $N = 1, 2, 3$ (green crosses on Fig. 7) are summarized in Table 1.

Table 1. Maxima of photonic enhancement factor with corresponding radii and iQE, for 1,2 and 3 layers.

N	$G_{phot}^{Max}[\%]$	$R_{Max}[nm]$	$\eta[\%]$
1	6.4	175	88.6
2	4.3	50	79.3
3	3.6	200	96.7

From the results, we can clearly recognize the benefit of photonic structuring of the photo-active layer. If the radius of the spheres is bigger than 100 nm, the photonic enhancement factor remains at least bigger than 1%. It is worth mentioning that the champion configuration for $N = 1$ ($R = 175$ nm) is close to the optimum found in ref [36] ($R = 200$ nm). Furthermore, the quasi-guided modes that were evidenced in 2D periodic array of holes inside perovskite by Smager and co-workers led to similar enhancement effect as the one reported here using opal-like structuring

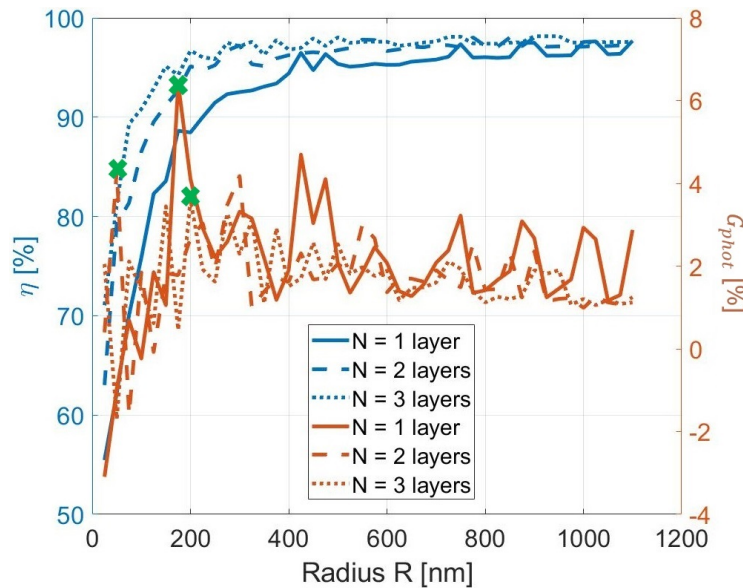


Fig. 7. Integrated quantum efficiency η (left) and photonic enhancement factor G_{phot} (right) as a function of the number of layers ($N = 1$ full lines, $N = 2$ dashed lines, $N = 3$ dotted lines), and with the radius R of the spheres as parameter. Green crosses correspond to the champion configurations as far as the photonic enhancement factor is concerned (Table 1).

[40,41]. Nevertheless, one should not forget the importance of parasitic absorption in PSC. This aspect will be the scope of a forthcoming study.

A detailed balance analysis [55,56] of our champion configuration for $N = 1$ was performed using the procedure described by Sandhu and coworkers [55]. The values we obtained for the short-circuit current J_{SC} , the open-circuit voltage V_{OC} and the PCE were, respectively, $J_{SC} = 23.94 \text{ mA/cm}^2$, $V_{OC} = 1.29 \text{ V}$, $PCE = 27.91\%$. These predictions must be regarded as largely optimistic ones since our calculation did not include non-radiative recombination and generation rates. Both optical and electrical imperfections in the fabrication of the opal-like perovskite film are expected to cause a substantial reduction of the efficiency.

4.4. Angular dependence

In the previous sections, we demonstrated the effects of photonic structuring in view to improve the PSC efficiency via light management. The different configurations showing optimal photonic enhancement factor were summarized in Table 1. We examine here the iQE angular dependence of these optimal configurations as well as of an unstructured PSC with a 600 nm-thick perovskite layer (section 4.1). Unpolarized incident light is considered by averaging for s and p polarizations. From the results shown in Fig. 8, iQE is found to be pretty stable regarding angular variations up to 60 degrees. For higher incidence angles, iQE decreases due to Fresnel reflections at the FTO interface, since the ability to couple light inside the structure is reduced and it becomes difficult to excite quasi-guided resonances. One should however note that the stability of iQE for unpolarized light comes from higher iQE for p polarization than for s polarization, especially at high incidence angle (not shown here). Indeed, the Brewster angle prevents light reflection and consequently allows more light to be absorbed within the structure. This angular behaviour has been observed elsewhere [57]. Finally, the robustness of the designed PSC regarding angular dependence is confirmed since the reported iQE are all superior to 40% up to grazing incidence.

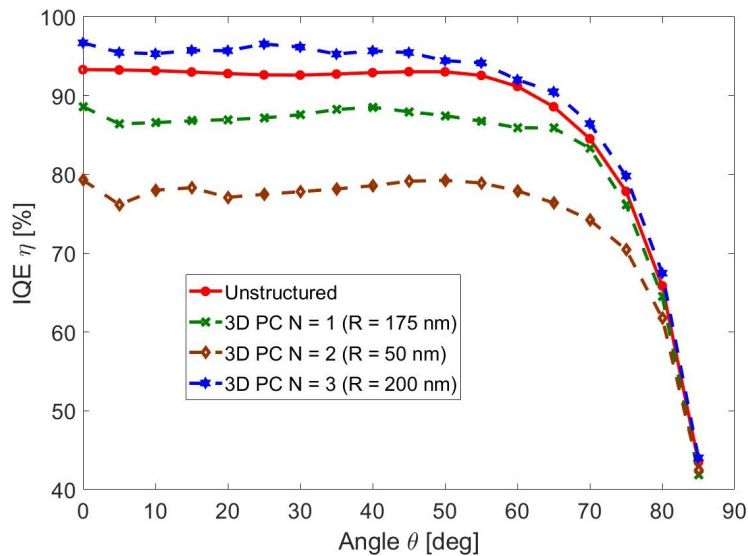


Fig. 8. Integrated quantum efficiency η as function of incidence angle θ for unpolarized light, in case of unstructured layer (600 nm perovskite) (red dots), a 3D PSC with 1 layer of spheres of radius $R = 175\text{nm}$ (green crosses), a 3D PSC with 2 layers of spheres of radius $R = 50\text{nm}$ (brown diamonds) and a 3D PSC with 3 layers of spheres of radius $R = 200\text{nm}$ (blue stars). Those cases correspond to the champion configurations reported in Table 1.

5. Conclusions

The effect of photonic structuring of the photo-active layer of a perovskite solar cell was numerically investigated. The positive impact of an opal-like arrangement of perovskite spheres was predicted through a photonic enhancement factor as high as 6.4% compared to an unstructured perovskite layer. This enhancement corresponds to 6.4% supplementary generated photo-electrons, if one supposes that each photon generates one electron-hole pair and increases in such a way the integrated photon efficiency. Moreover, the photonic enhancement factor is positive and always bigger than 1% if the radius of the spheres is bigger than 100 nm. The physical mechanism behind the enhancement of the absorptance is the excitation of quasi-guided modes inside the photonic structures, via Fano resonances excitation. Nevertheless, the parasitic absorption present in the other layers (FTO, TiO_2 and gold layers) was thoroughly analyzed and found to be non-negligible. This parasitic absorption partly reduces the internal quantum efficiency and the generation of electron-holes pairs. Finally, the angular dependence of the internal quantum efficiency is robust up to an incidence angle of 60 degrees. Those results demonstrate a promising way to exploit photonic structuring in the context of perovskite solar cells. The remaining challenges are, among others, the reduction of the energy loss due to Fresnel reflection using an anti-reflective coating, the optimization of the layer thicknesses to foster light absorption inside the photo-active layer and the decrease of the inevitable parasitic absorption inside the layers adjacent to the photo-active layer.

Funding

Fédération Wallonie-Bruxelles (grant for Concerted Research Actions).

Acknowledgments

The authors would like to thank P. Barzin for his graphical support, D. Collignon, P. Lovat and F. Collard for their computational support.

Disclosures

The authors declare no conflicts of interest.

References

1. "Best Research-Cell Efficiency Chart | Photovoltaic Research | NREL, <https://www.nrel.gov/pv/cell-efficiency.html>, 2019-06-05,".
2. S. Basu Mallick, N. P. Sergeant, M. Agrawal, J.-Y. Lee, and P. Peumans, "Coherent light trapping in thin-film photovoltaics," *MRS Bull.* **36**(6), 453–460 (2011).
3. M. L. Brongersma, Y. Cui, and S. Fan, "Light management for photovoltaics using high-index nanostructures," *Nat. Mater.* **13**(5), 451–460 (2014).
4. F. Priolo, T. Gregorkiewicz, M. Galli, and T. F. Krauss, "Silicon nanostructures for photonics and photovoltaics," *Nat. Nanotechnol.* **9**(1), 19–32 (2014).
5. X. Meng, V. Depauw, G. Gomard, O. E. Daif, E. Drouard, C. Jamois, A. Fave, F. Dross, I. Gordon, and C. Seassal, "Design, fabrication and optical characterization of photonic crystal assisted thin film monocrystalline-silicon solar cells," *Opt. Express* **20**(S4), A465–A475 (2012).
6. J. D. Joannopoulos, *Photonic crystals : molding the flow of light* (Princeton University, 2008).
7. X. Sheng, L. Z. Broderick, and L. C. Kimerling, "Photonic crystal structures for light trapping in thin-film Si solar cells : Modeling, process and optimizations," *Opt. Commun.* **314**, 41–47 (2014).
8. R. B. Wehrspohn and J. Üpping, "3D photonic crystals for photon management in solar cells," *J. Opt.* **14**(2), 024003 (2012).
9. Y. Tanaka, Y. Kawamoto, M. Fujita, and S. Noda, "Enhancement of broadband optical absorption in photovoltaic devices by band-edge effect of photonic crystals," *Opt. Express* **21**(17), 20111–20118 (2013).
10. A. Mihi, M. E. Calvo, J. A. Anta, and H. Mi, "Spectral Response of Opal-Based Dye-Sensitized Solar Cells," *J. Phys. Chem. C* **112**(1), 13–17 (2008).
11. A. Mihi and H. Mi, "Origin of Light-Harvesting Enhancement in Colloidal-Photonic-Crystal-Based Dye-Sensitized Solar Cells," *J. Phys. Chem. B* **109**(33), 15968–15976 (2005).
12. L. Ha, M. Ocan, B. S. Colodrero, G. Boschloo, and A. Hagfeldt, "Porous One-Dimensional Photonic Crystals Improve the Power-Conversion Efficiency of Dye-Sensitized Solar Cells," *Adv. Mater.* **21**(7), 764–770 (2009).
13. G. Lozano, S. Colodrero, O. Caulier, M. E. Calvo, and V. Se, "Theoretical Analysis of the Performance of One-Dimensional Photonic Crystal-Based Dye-Sensitized Solar Cells," *J. Phys. Chem. C* **114**(8), 3681–3687 (2010).
14. S. Guldin, S. Huttner, M. Kolle, M. E. Welland, P. Müller-Buschbaum, R. H. Friend, U. Steiner, and N. Tetreault, "Dye-sensitized solar cell based on a three-dimensional photonic crystal," *Nano Lett.* **10**(7), 2303–2309 (2010).
15. U. Fano, "Effects of Configuration Interaction on Intensities and Phase Shifts," *Phys. Rev.* **124**(6), 1866–1878 (1961).
16. M. F. Limonov, M. V. Rybin, A. N. Poddubny, and Y. S. Kivshar, "Fano resonances in photonics," *Nat. Photonics* **11**(9), 543–554 (2017).
17. S. Campione, D. de Ceglia, C. Guclu, M. A. Vincenti, M. Scalora, and F. Capolino, "Fano collective resonance as complex mode in a two-dimensional planar metasurface of plasmonic nanoparticles," *Appl. Phys. Lett.* **105**(19), 191107 (2014).
18. N. Sharac, H. Sharma, M. Veysi, R. N. Sanderson, M. Khine, F. Capolino, and R. Ragan, "Tunable optical response of bowtie nanoantenna arrays on thermoplastic substrates," *Nanotechnology* **27**(10), 105302 (2016).
19. M. V. Rybin, A. B. Khanikaev, M. Inoue, K. B. Samusev, M. J. Steel, G. Yushin, and M. F. Limonov, "Fano Resonance between Mie and Bragg Scattering in Photonic Crystals," *Phys. Rev. Lett.* **103**(2), 023901 (2009).
20. M. F. Limonov and R. M. De La Rue, *Optical properties of photonic structures : interplay of order and disorder* (CRC, 2012).
21. Y. A. Vlasov, X.-Z. Bo, J. C. Sturm, and D. J. Norris, "On-chip natural assembly of silicon photonic bandgap crystals," *Nature* **414**(6861), 289–293 (2001).
22. M. V. Rybin, K. B. Samusev, I. S. Sinev, G. Semouchkin, E. Semouchkina, Y. S. Kivshar, and M. F. Limonov, "Mie scattering as a cascade of Fano resonances," *Opt. Express* **21**(24), 30107–30113 (2013).
23. A. N. Poddubny, M. V. Rybin, M. F. Limonov, and Y. S. Kivshar, "Fano interference governs wave transport in disordered systems," *Nat. Commun.* **3**(1), 914 (2012).
24. M. I. Tribelsky and A. E. Miroshnichenko, "Giant in-particle field concentration and Fano resonances at light scattering by high-refractive-index particles," *Phys. Rev. A* **93**(5), 053837 (2016).
25. S. E. Han and G. Chen, "Optical Absorption Enhancement in Silicon Nanohole Arrays for Solar Photovoltaics," *Nano Lett.* **10**(3), 1012–1015 (2010).
26. S. B. Mallick, M. Agrawal, and P. Peumans, "Optimal light trapping in ultra-thin photonic crystal crystalline silicon solar cells," *Opt. Express* **18**(6), 5691–5706 (2010).

27. D. H. Ko, J. R. Tumbleston, L. Zhang, S. Williams, J. M. Desimone, R. Lopez, and E. T. Samulski, "Photonic Crystal Geometry for Organic Solar Cells," *Nano Lett.* **9**(7), 2742–2746 (2009).
28. D. Duché, C. Masclaux, J. Le Rouzo, and C. Gourgon, "Photonic crystals for improving light absorption in organic solar cells," *J. Appl. Phys.* **117**(5), 053108 (2015).
29. A. Kojima, K. Teshima, T. Miyasaka, and Y. Shirai, "Novel Photoelectrochemical Cell with Mesoscopic Electrodes Sensitized by Lead-Halide Compounds (2)," Meeting Abstracts **MA2006-0**, 397 (2006).
30. M. A. Green, Y. Jiang, A. M. Soufiani, and A. Ho-Baillie, "Optical Properties of Photovoltaic Organic–Inorganic Lead Halide Perovskites," *J. Phys. Chem. Lett.* **6**(23), 4774–4785 (2015).
31. L. Lang, J.-H. Yang, H.-R. Liu, H. Xiang, and X. Gong, "First-principles study on the electronic and optical properties of cubic ABX₃ halide perovskites," *Phys. Lett. A* **378**(3), 290–293 (2014).
32. M. Shirayama, H. Kadowaki, T. Miyadera, T. Sugita, M. Tamakoshi, M. Kato, T. Fujiseki, D. Murata, S. Hara, T. N. Murakami, S. Fujimoto, M. Chikamatsu, and H. Fujiwara, "Optical Transitions in Hybrid Perovskite Solar Cells: Ellipsometry, Density Functional Theory, and Quantum Efficiency Analyses for CH₃NH₃PbI₃," *Phys. Rev. Appl.* **5**(1), 014012 (2016).
33. P. Löper, M. Stuckelberger, B. Niesen, J. Werner, M. Filipič, S.-J. Moon, J.-H. Yum, M. Topič, S. De Wolf, and C. Ballif, "Complex Refractive Index Spectra of CH₃NH₃PbI₃ Perovskite Thin Films Determined by Spectroscopic Ellipsometry and Spectrophotometry," *J. Phys. Chem. Lett.* **6**(1), 66–71 (2015).
34. S. Schünemann, K. Chen, S. Brittman, E. Garnett, and H. Tüysüz, "Preparation of Organometal Halide Perovskite Photonic Crystal Films for Potential Optoelectronic Applications," *ACS Appl. Mater. Interfaces* **8**(38), 25489–25495 (2016).
35. K. Meng, S. Gao, L. Wu, G. Wang, X. Liu, G. Chen, Z. Liu, and G. Chen, "Two-Dimensional Organic–Inorganic Hybrid Perovskite Photonic Films," *Nano Lett.* **16**(7), 4166–4173 (2016).
36. B.-X. Chen, H.-S. Rao, H.-Y. Chen, W.-G. Li, D.-B. Kuang, and C.-Y. Su, "Ordered macroporous CH₃NH₃PbI₃ perovskite semitransparent film for high-performance solar cells," *J. Mater. Chem. A* **4**(40), 15662–15669 (2016).
37. S.-J. Ha, J. H. Heo, S. H. Im, and J. H. Moon, "Mesoscopic CH₃NH₃PbI₃ perovskite solar cells using TiO₂ inverse opal electron-conducting scaffolds," *J. Mater. Chem. A* **5**(5), 1972–1977 (2017).
38. K. Chen and H. Tüysüz, "Morphology-Controlled Synthesis of Organometal Halide Perovskite Inverse Opals," *Angew. Chem., Int. Ed.* **54**(46), 13806–13810 (2015).
39. J. Dewalque, C. Henrist, and J. Loicq, "Light-harvesting capabilities of dielectric sphere multilayers," *Photonic and Phononic Properties of Engineered Nanostructures VIII*, A. Adibi, S.-Y. Lin, and A. Scherer, eds. (SPIE, 2018), p. 72.
40. R. Schmagier, I. Hossain, F. Schackmar, B. Richards, G. Gomard, and U. Paetzold, "Light coupling to quasi-guided modes in nanoimprinted perovskite solar cells," *Sol. Energy Mater. Sol. Cells* **201**, 110080 (2019).
41. R. Schmagier, G. Gomard, B. S. Richards, and U. W. Paetzold, "Nanophotonic perovskite layers for enhanced current generation and mitigation of lead in perovskite solar cells," *Sol. Energy Mater. Sol. Cells* **192**, 65–71 (2019).
42. M. Saliba, J.-P. Correa-Baena, C. M. Wolff, M. Stollerfoht, N. Phung, S. Albrecht, D. Neher, and A. Abate, "How to Make over 20% Efficient Perovskite Solar Cells in Regular n-i-p and Inverted p-i-n Architectures," *Chem. Mater.* **30**(13), 4193–4201 (2018).
43. J. M. Ball, S. D. Stranks, M. T. Hörantner, S. Hüttner, W. Zhang, E. J. W. Crossland, I. Ramirez, M. Riede, M. B. Johnston, R. H. Friend, and H. J. Snaith, "Optical properties and limiting photocurrent of thin-film perovskite solar cells," *Energy Environ. Sci.* **8**(2), 602–609 (2015).
44. R. L. Olmon, B. Slovick, T. W. Johnson, D. Shelton, S. H. Oh, G. D. Boreman, and M. B. Raschke, "Optical dielectric function of gold," *Phys. Rev. B: Condens. Matter Mater. Phys.* **86**(23), 235147 (2012).
45. I. Hussain, H. P. Tran, J. Jaksik, J. Moore, N. Islam, and M. J. Uddin, "Functional materials, device architecture, and flexibility of perovskite solar cell," *Emergent Mater.* **1**(3-4), 133–154 (2018).
46. M. G. Moharam and T. K. Gaylord, "Rigorous coupled-wave analysis of planar-grating diffraction," *J. Opt. Soc. Am.* **71**(7), 811 (1981).
47. M. Lobet, M. Lard, M. Sarrazin, O. Deparis, and L. Henrard, "Plasmon hybridization in pyramidal metamaterials: a route towards ultra-broadband absorption," *Opt. Express* **22**(10), 12678 (2014).
48. We used here iQE with a lower case for our integrated quantum efficiency (photonic quantity) in order to avoid any confusion with IQE usually referred as internal quantum efficiency. The later includes the number of electron collected by a solar cell, is consequently an electric quantity and we do not aim to characterize the electric properties of the PSC in the present study.
49. A. Herman, C. Trompoukis, V. Depauw, O. E. Daif, and O. Deparis, "Influence of the pattern shape on the efficiency of front-side periodically patterned ultrathin crystalline silicon solar cells," *J. Appl. Phys.* **112**(11), 113107 (2012).
50. A. Lin and J. Phillips, "Optimization of random diffraction gratings in thin-film solar cells using genetic algorithms," *Sol. Energy Mater. Sol. Cells* **92**(12), 1689–1696 (2008).
51. K.-H. Brenner, "Aspects for calculating local absorption with the rigorous coupled-wave method," *Opt. Express* **18**(10), 10369 (2010).
52. S. Fan and J. Joannopoulos, "Analysis of guided resonances in photonic crystal slabs," *Phys. Rev. B* **65**(23), 235112 (2002).
53. S. Peng and G. M. Morris, "Experimental demonstration of resonant anomalies in diffraction from two-dimensional gratings," *Opt. Lett.* **21**(8), 549 (1996).

54. M. Lopez-Garcia, J. Galisteo-Lopez, C. Lopez, and A. Garcia-Martin, "Light confinement by two-dimensional arrays of dielectric spheres," *Phys. Rev. B: Condens. Matter Mater. Phys.* **85**(23), 235145 (2012).
55. S. Sandhu, Z. Yu, and S. Fan, "Detailed balance analysis of nanophotonic solar cells," *Opt. Express* **21**(1), 1209 (2013).
56. W. E. Sha, X. Ren, L. Chen, and W. C. Choy, "The efficiency limit of CH₃NH₃PbI₃ perovskite solar cells," *Appl. Phys. Lett.* **106**(22), 221104 (2015).
57. M. Lobet, N. Reckinger, L. Henrard, and P. Lambin, "Robust electromagnetic absorption by graphene/polymer heterostructures," *Nanotechnology* **26**(28), 285702 (2015).